Electronic Supplementary Information

Core-shell ZnO@C:N hybrids derived from MOFs as long-cycling anodes for lithium ion batteries

Yichuan Guo[a], Zhaoying Wang[b], Xinsheng Lu[a], Jianguo Lu*[ab], Rabia Khatoon[a], Hongwen Chen[a], Rui Hu[a], Haichao Tang[a], Qinghua Zhang[bc], and Zhoupeng Li*[bc]

[a] State Key Laboratory of Silicon Materials, School of Materials Science and Engineering, Zhejiang University, Hangzhou 310027, China. E-mail: lujianguo@zju.edu.cn

[b] Ningbo Research Institute, Zhejiang University, Ningbo 315100, China.

[c] College of Chemical and Biological Engineering, Zhejiang University, Hangzhou 310027, China. E-mail: zhoupengli@zju.edu.cn

Contents

Experimental Sections

1. Synthesis of ZnO@C:N and ZnO@C hybrids. Zinc-glycolate MOFs precursor was synthesized via a hydrothermal method. Zinc nitrate (10 mmol) and glycolic acid (10 mmol) were successively added into 20 ml ethanol in a breaker. After sonication, both zinc nitrate and glycolic acid were dissolved to form transparent solution. The mixture was transferred into a 20 ml capless glass bottle. Then the glass bottle was put into a 50 mL Teflon autoclave. Heating treatment of the mixture at 160 °C for 16 h was done to yield the intermediate product. The product was centrifugal treatment by ethanol and deionized water alternately for three times and then dried in an oven at 80 °C for 12 h. Then, the brown precursor of nitrogen-doped zinc-glycolate MOFs (named as Zn-GA:N) were obtained. The carbonization of Zn-GA:N was typically carried out at 500 °C for 4 h in argon atmosphere at a heating rate of 2 °C min^{-1}, followed by being cooled to room temperature naturally. The final black product was the ZnO@C:N.

For comparison, the ZnO@C was also synthesized in a similar process, with an except that the reactant of zinc nitrate was substituted by zinc acetate. The obtained white precursor was zinc-glycolate MOFs (named as Zn-GA) and the final black product was the ZnO@C hybrid.

2. Assembly of lithium-ion batteries. In a typical LiB assembly, ZnO@C:N as active anode material, polyvinylidene fluoride (PVDF) as binder and super P as conductive agent were mixed at a mass ratio of 8:1:1. The mixture was ground in the solvent of N-Methyl pyrrolidone (NMP) and the obtained slurry was coated on a

copper foil uniformly. Then the copper foil covered by electrode material was put in an oven at 60 °C for 12 h to get dried and cut into wafers with a diameter of 16 mm and used as the ZnO@C:N anode. Also, the ZnO@C hybrid and commercial ZnO electrodes were prepared in the same way for comparison. The above electrodes were assembled in CR 2032-type coin batteries. The lithium metal foils work as the counter electrodes. Porous polypropylene membrane was used as the separator and 1M LiPF$_6$ in dimethyl carbonate/ethylene carbonate (DMC/EC, with the volume ratio of 1:1) solution as the electrolyte. All batteries are packed in an argon-atmosphere glove box with both moisture and oxygen content less than 0.1 ppm.

3. Material Characterization. The ZnO@C:N and ZnO@C hybrids were investigated for phase analysis by X-ray diffraction (XRD) with Cu Kα radiation (λ=1.5406 Å) in the diffraction angle range of 10-80°. Thermal gravimetric analysis (TGA) were characterized in air with a SDTQ600V20.9 themogravimetric analyzer, with temperature range from 20 °C to 600 °C and the heating rate was 10 °C min^{-1}. The morphology of ZnO@C:N and ZnO@C were identified by scanning electron microscopy (SEM, S-4800, Hitachi) and microstructure of ZnO@C:N was characterized high-resolution transmission electron microscopy (HRTEM, FEIF20). The elemental distribution and composition were characterized by energy dispersive X-ray spectroscopy (EDX) attached to TEM. X-ray photoelectron spectroscopy (XPS) spectra were used to analyze the valency states of elements with a Thermo Escalab 250XI spectrometer. Raman spectra were conducted with a HORIBA HR-800 spectrometer using a 514 nm He-Ne laser. The specific surface area and pore size

distribution were characterized by the nitrogen adsorption desorption tests were obtained with a Micromeritics ASAP2020 analyzer at 77 K.

4. Electrochemical measurements. All the electrochemical tests were performed in a room at 25 °C. The galvanostatic charge-discharge (GCD) curves were recorded with a LAND CT2001A battery test system at different current densities in a voltage range of 0.1-3 V vs. Li^+/Li. The electrochemical impedance spectroscopy (EIS) measurement was conducted with a CHI 760E workstation. All the EIS measurements were tested in the frequency range of $10^{-2} - 10^{5}$ Hz with the amplitude of 5 mV at open circuit voltage. Cyclic voltammograms (CV) profiles were obtained on a CHI 760E workstation at a scan rate of 0.5 mV s^{-1} from 0.1 V vs. Li^+/Li to 3.0 V vs. Li^+/Li. All the specific capacities were calculated only according the mass of active materials in anode.

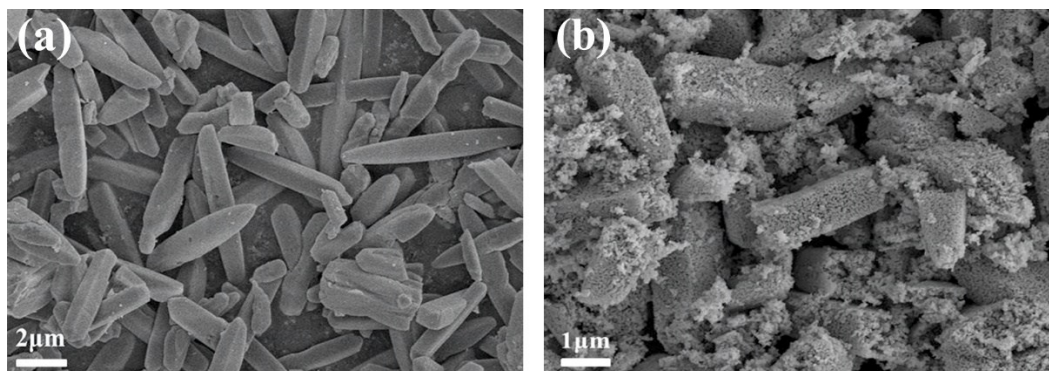# Supplementary Figures (Figure S1 to Figure S9)

Figure S1. SEM images of (a) Zn-GA precursor and (b) ZnO@C hybrid

As displayed in **Fig. S1a**, the Zn-GA precursor has a double quadrangular pyramid morphology with a side length of ~10 μm. After pyrolyzation, the ZnO@C quadrangular pyramids are ~2μm in length and constituted of interconnected core-shell nanoparticles with a diameter of around 50-100 nm (**Fig. S1b**).
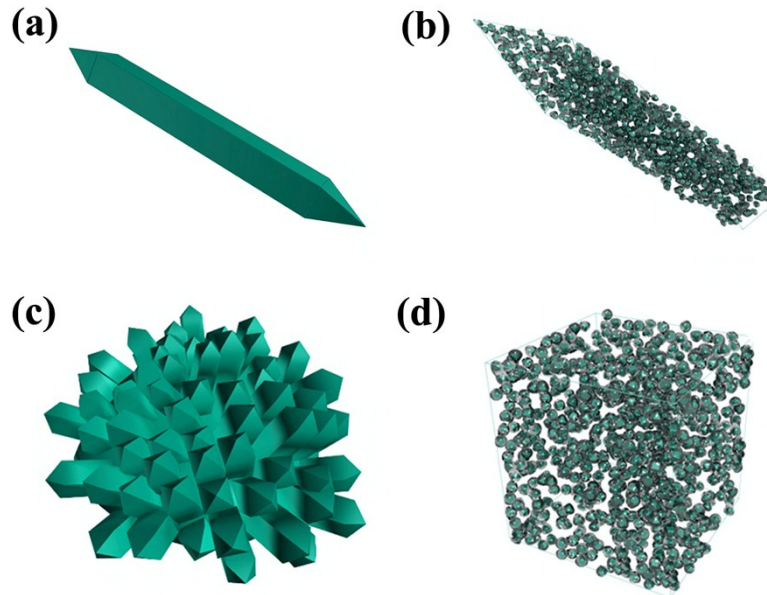
Figure S2. Structure schematics of (a) Zn-GA, (b) ZnO@C, (c) Zn-GA:N and (d) ZnO@C:N.

The morphological evolution from the Zn-GA and Zn-GA: N precursors to the corresponding pyrolysis products are schematically illustrated in **Fig. S2**. During pyrolysis, Zn^{2+}, glycolate and nitrogen-doped glycolate convert to ZnO nanoparticles, carbon shells and N-doped carbon shells, respectively. After pyrolysis, the ZnO@C hybrid mostly remains the original quadrangular pyramid morphology of Zn-GA precursor, while the initial polyhedron shape of Zn-GA:N precursor transforms to the interconnected nanoparticle morphology of ZnO@C:N hybrid. Evidently, the hierarchical multi-porous nanostructures have been formed for both ZnO@C and ZnO@C:N hybrids, which makes them highly accessible to electrolyte for energy storage.
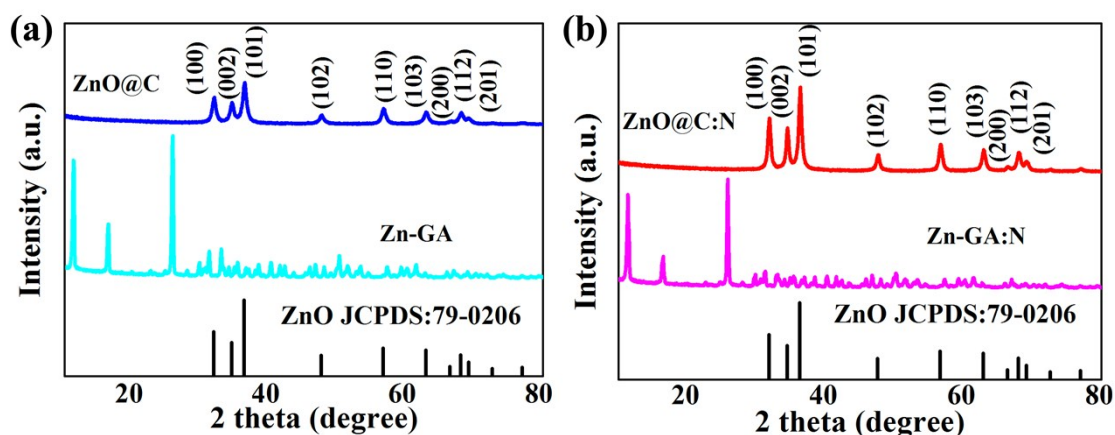
Figure S3. XRD spectra of (a) Zn-GA and ZnO@C, (b) Zn-GA:N and ZnO@C:N.

As shown in **Fig. S3**, both Zn-GA and Zn-GA:N have almost the same XRD appearances. The sharp diffraction peaks located at 11.2, 16.3 and 25.7° are in good match with those previously reported in the MOF of Zn-GA:N.[S1] It seems that the Zn-GA and Zn-GA:N have the same crystalline structure, although they are very different in shape. After pyrolysis, hybrid products are both obtained for Zn-GA and Zn-GA:N precursors. The XRD patterns of ZnO@C and ZnO@C:N are also very similar. The characteristic peaks located at 31.7, 34.4, 36.2, 47.4, 56.5, 62.9, 66.4, 67.9 and 72.6° can be identified as (100), (002), (101), (102), (110), (103), (200), (112) and (201) planes of wurtzite-type ZnO, respectively. The characteristic peaks of both of ZnO@C and ZnO@C:N can be attributed to wurtzite-type ZnO (JCPDS No. 79-0206). No diffraction peaks from carbon are observed, suggesting that they are both amorphous for the carbon shell in ZnO@C hybrid and nitrogen-doped carbon shell in ZnO@C:N hybrid. The XRD results verify the successful carbonization of Zn-GA and Zn-GA:N precursors to form ZnO@C and ZnO@C:N hybrids.
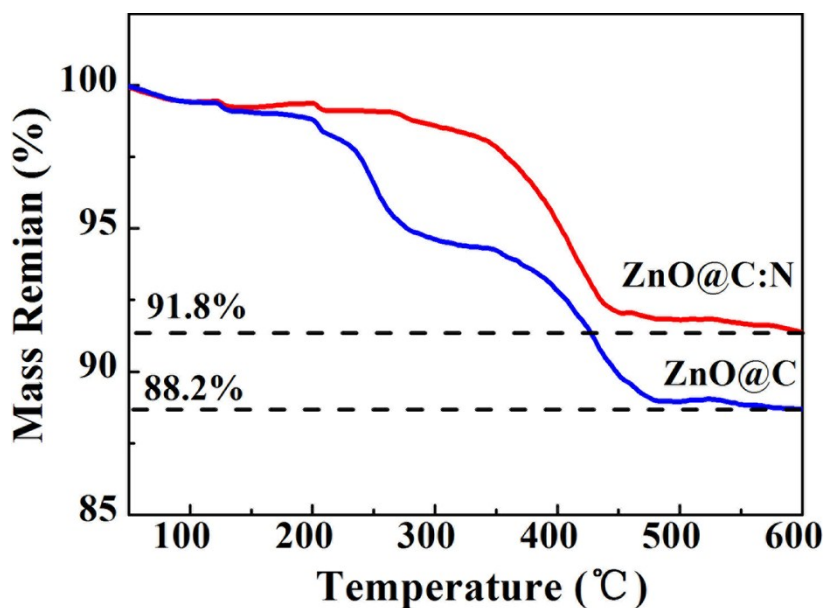
Figure S4. Thermogravimetric analysis of ZnO@C and ZnO@C:N hybrids.

Fig. S4 shows the TGA data for both ZnO@C:N and ZnO@C core-shell hybrids. The mass losses in the temperature range of 25-200 °C and 350-500 °C can be attributed to the evaporation of combined water and the oxidation of carbon, respectively.[S2] Remarkably, the obvious mass loss of ZnO@C in the range of 200-300 °C is assigned to oxidation of the unbonded carbon, whereas this mass drop is absent for ZnO@C:N in the same temperature region. This observation reveals that the introduction of nitrogen atoms into the carbon shells strengthens the bonding between the ZnO core and nitrogen-doped carbon shell. When the temperature above 500 °C, full oxidation of carbon happens with only ZnO left. The content of ZnO is calculated to be 91.8 wt.% and 88.2 wt.% in the ZnO@C:N and ZnO@C hybrids, respectively. Evidently, the ZnO@C:N hybrid has a higher ZnO content. Moreover, these results reveal that the structure of the ZnO@C:N hybrids is more stable than that of ZnO@C hybrids.
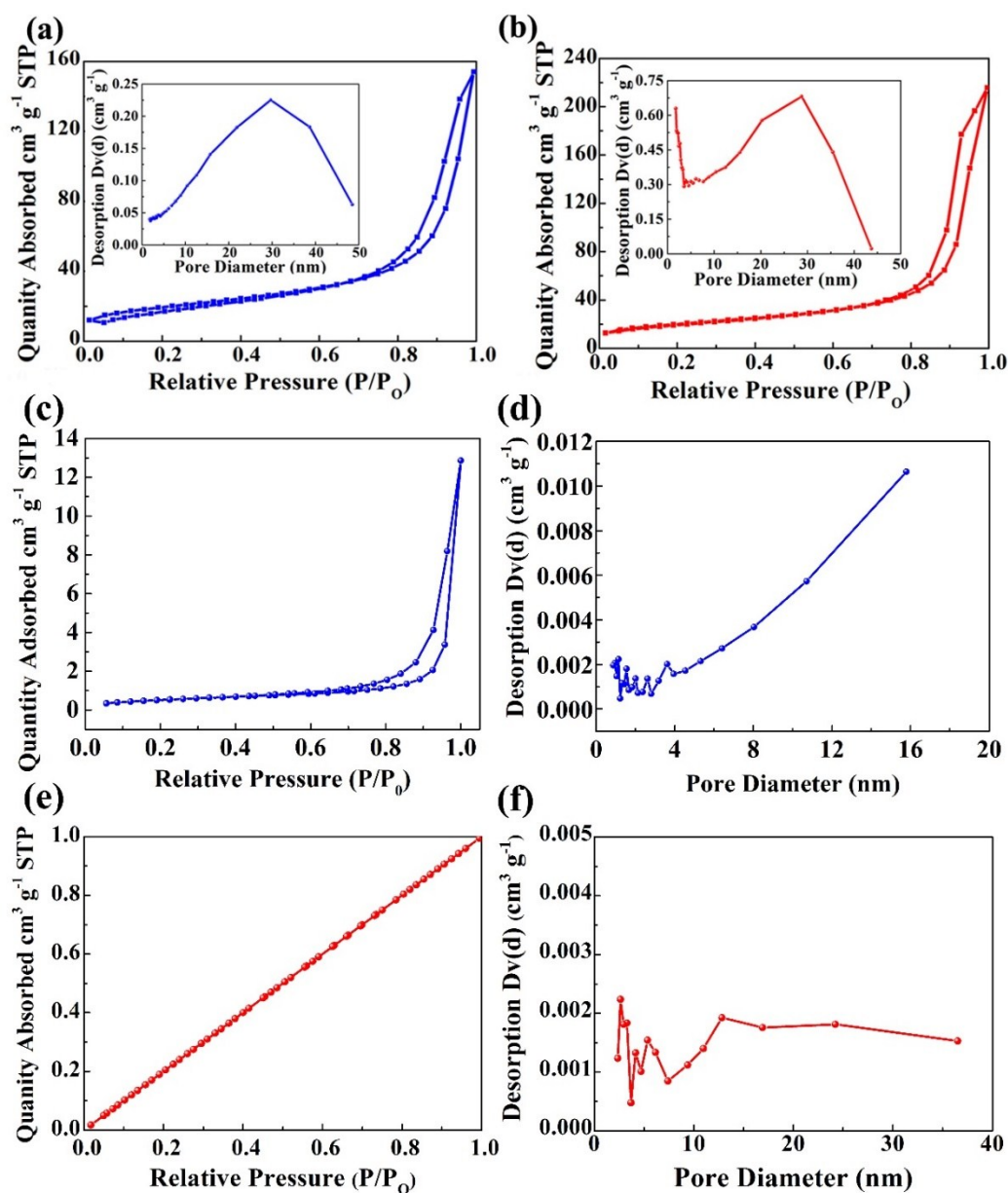
Figure S5. BET data of (a) ZnO@C and (b) ZnO@C:N. (c) Nitrogen absorption/desorption curves of Zn-GA and (d) pore size distribution of Zn-GA. (e) Nitrogen absorption/desorption curves of Zn-GA:N and (f) pore size distribution of Zn-GA:N.

Nitrogen absorption and desorption test was undertaken to characterize the specific area and the pore diameter of Zn-GA:N precursor, ZnO@C and ZnO@C:N. **Fig S5a,b** show the corresponding type-IV adsorption/desorption isotherms. The specific surface areas of for the ZnO@C and ZnO@C:N hybrids are calculated by the

Brunauer–Emmett–Teller (BET) method to be 68.1 and 74.8 m^2 g^{-1}. The ZnO@C:N hybrid is mesoporous with a wide pore size distribution centered at ~30 nm and also microporous with a diameter below 2 nm. In contrast, the ZnO@C hybrid only shows mesoporosity with a wide pore size distribution in the 10–50 nm. The ZnO@C:N hybrid has a slightly higher specific surface area than the ZnO@C, which can be ascribed to the following two reasons: (1) ZnO@C:N has a smaller particle size than ZnO@C due to the stronger anchoring of ZnO on the surface of nitrogen-doped carbon shells; (2) The introduction of nitrogen atoms results in higher defect density of into carbon shell within ZnO@C:N hybrid. The mesoporosity and microporosity of ZnO@C:N can be attributed to the channels between core-shell nanoparticles and the defects caused by the doped nitrogen atoms, respectively. There is a type-IV adsorption/desorption isotherm in **Fig. S5c**. And **Fig. S5d** shows that there are some micropores in Zn-GA. The specific area of Zn-GA calculated by BET method is 2.1 m^2g^{-1}. It is confirmed that the mesopores in ZnO@C are formed after carbonization. As shown in **Fig. S5e**, there is no difference between the nitrogen absorption and desorption processes, which can be ascribed to the low specific area of 1.97m^2 g^{-1} according to the BET result. The low specific area indicates the relatively smooth surface of Zn-GA:N, as evidenced by the SEM images. **Fig. S5f** shows the pore diameter distribution of Zn-GA:N. The mesopores have a mean diameter centered at ~13 nm. And the diameter of micropores falls below 5 nm in Zn-GA:N. It was confirmed that the micropores and mesopores in ZnO@C:N are formed after carbonization.
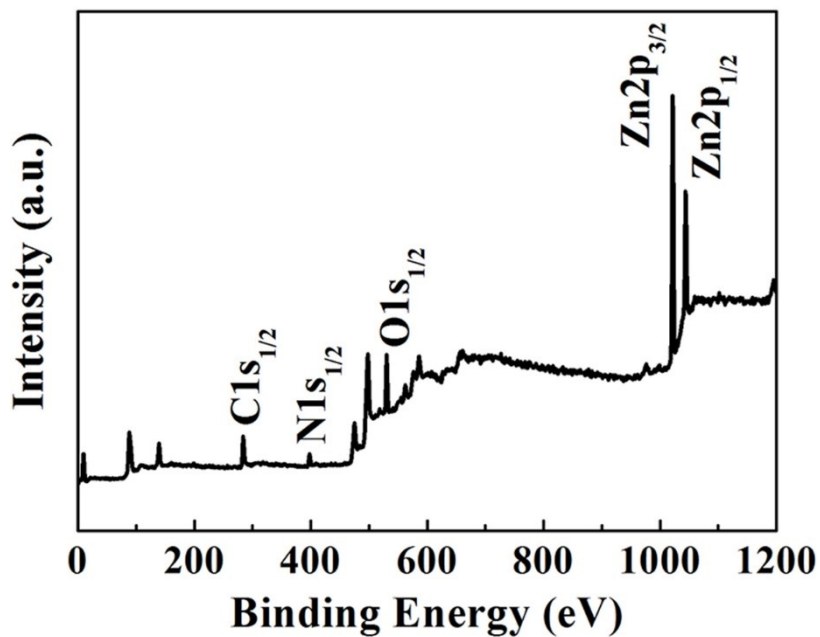
Figure S6. Full XPS spectrum of ZnO@C:N.

XPS analysis is conducted to investigate the chemical states and the bond types of nitrogen in ZnO@C:N hybrid. There are C, N, O and Zn elements in ZnO@C:N hybrid shown in **Fig. S6**.
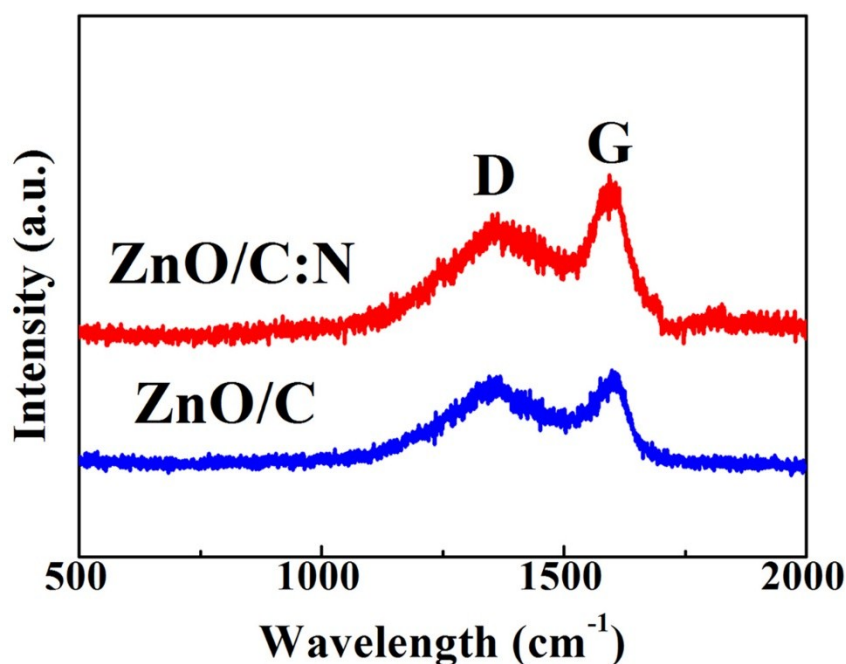
Figure S7. Raman spectra of ZnO@C:N and ZnO@C.

The graphitization degrees of carbon in ZnO@C:N and ZnO@C hybrids are characterized by Raman spectroscopy. **Fig. S7** presents the Raman spectra of ZnO@C:N and ZnO@C in the wavenumber of 500-2000 cm^{-1}, where the two dominant peaks ~1333 and ~1580 cm^{-1} are ascribed to D and G bands of carbon, respectively.[S3] The intensity ratio of G-band to D-band (I_D/I_G) can be an indicator of the graphitization degree of carbon materials. The I_D/I_G value is determined to be 1.41 for ZnO@C:N, which is higher than that of ZnO@C (1.26). This result illustrates that the ZnO@C:N hybrid has a lower degree of graphitization than the ZnO@C hybrid. Therefore, it can be inferred that the nitrogen doping leads to a higher density of carbon lattice defects. These defects may provide abundant active sites for lithialaion/delithialation to increase the specific capacity of ZnO@C:N anode.
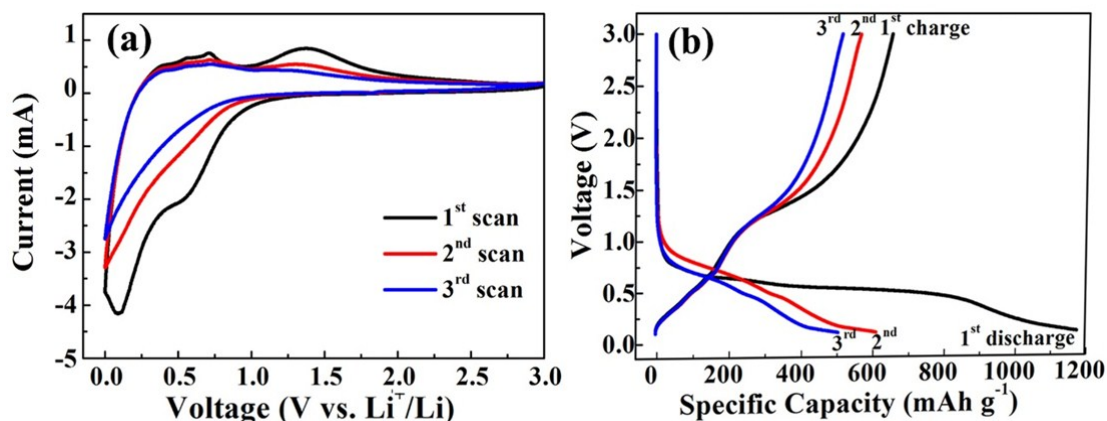
Figure S8 (a) CV curves of ZnO@C at a scan rate of 0.5mV s^{-1} in the voltage range of 0.1-3V; (b) Discharge/charge curves of ZnO@C for the 1st, 2nd and 3rd cycles at a current density of 0.1 A g^{-1}.

CV curves in **Fig. S8a** are recorded to investigate the redox properties of the ZnO@C hybrid. The cathodic peak is located at ~0.7 V *vs.* Li$^+$/Li in the first discharging process, corresponding to the reduction of zinc ions to Zn metal and the appearance of solid electrolyte interphases (SEI) films.[S4,S5] This cathodic peak only appears in the first cycle and gradually disappears in the following cycles, which means SEI mainly forms in the first discharging process.[S3,S6,S7] The cathodic peak located at ~0.2 V *vs.* Li$^+$/Li is mainly attributed to the alloying process of zinc and lithium to form Zn-Li alloy.[S7,S8] This cathodic peak decreases obviously in the successive 2nd and 3rd cycles for the ZnO@C hybrid. The anodic peaks in the voltage range of 0.2-0.7 V *vs.* Li$^+$/Li correspond to the multiple dealloying steps of Zn-Li alloy.[S3,S9] The anodic peak located at ~1.5 V *vs.* Li$^+$/Li results from the replacement reaction of zinc metal with lithium oxide to form zinc oxide and lithium,[S8,S10] which decay in some degree in the 2nd and 3rd cycles.

Fig. S8b shows GCD curves of ZnO@C hybrids in the first three cycles, recorded at 0.1 A g^{-1}. A long flat plateau in the first discharge process corresponding to the reduction of Zn^{2+} to Zn and the formation of SEI film.[S7] This plateau decreases obviously in the 2nd cycle for SEI film only forms in the first discharge process. Two small plateaus located at 0.28 and 0.65 V and one wide plateau centered at 1.3 V can be distinguished from the 1st charge curve. The former two plateaus are contributed to the multi-step delithiation of Zn-Li alloys to generate Zn metal and lithium ions, and the last plateau is attributed to the oxidation of Zn metal to ZnO.[S3] The GCD results are in good agreement with the CV curves. In the 3rd discharge process, the ZnO@C hybrid only remains 513 mAh g^{-1}, with a capacity retention of 43% (based on the initial capacity). The irreversible capacity loss during the first three cycles is accounted by the SEI formation accompanied by the consumption of lithium ions and electrolyte. For the ZnO@C:N hybrid (**Fig. 3b**), the specific capacity is reduced to 678 mAh g^{-1} in the 3rd cycle, with the capacity retention of 61% (based on the initial capacity). Therefore, the ZnO@C:N hybrid has better capacity retention compared with ZnO@C hybrid.

During the discharge process, the electrode reactions on ZnO accounting for the reversible discharge capacity are as equations (S1) and (S2),

$$ZnO + 2Li^+ 2e^- \rightarrow Zn + Li_2O \qquad \text{(S1)}$$

$$Zn + Li^+ + e^- \rightarrow LiZn \qquad \text{(S2)}$$
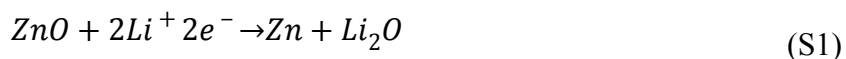
In the charging process, the reversible electrode reactions accounting for the charge

capacity are as equations (S3) and (S4),

$$LiZn \rightarrow Zn + Li^+ + e^-$$
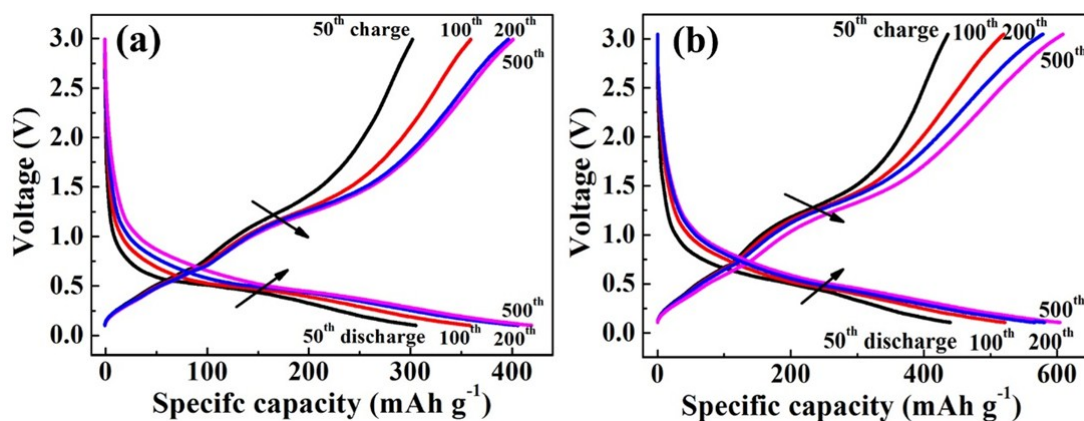
(S3)

$$Zn + Li_2O \rightarrow ZnO + 2Li^+ 2e^-$$

(S4)

Figure S9. Discharge/charge curves of (a) ZnO@C and (b) ZnO@C:N for the 50th, 100th, 200th and 500th cycles at a current density of 0.1 A g^{-1}.

Fig. S9 shows GCD curves of the 50th, 100 th, 200 th and 500 th cycle of the ZnO@C hybrid and ZnO@C:N hybrid. It should be noted that as the number of cycles increases, the lithiation potential moves up in the discharge process and the delithiation potential moves down in the charge process. The gradual change of potential contributes to the activation of ZnO which also corresponds to the capacity increase from 50th to 200th cycles in long-cycle performance in **Fig 3c**.

Supplementary Table

Table. S1 Contents of C, N, O and Zn in ZnO@C:N by TEM element mapping.

Element	Atomic percentage (%)
Carbon	32.32
Nitrogen	0.41
Oxygen	42
Zinc	25.27

The atomic contents of C, N, O and Zn are 32.32%, 0.41%, 42% and 25.27%, respectively according to TEM element mapping.

References

S1.   C. Shang, R. Gautier, T. Jiang, E. Faulques, C. Latouche, M. Paris, L. Cario, M. Bujoli-Doeuff and S. Jobic, *Inorganic chemistry*, 2017, **56**, 6208-6213.

S2.   C. Xiao, S. Zhang, S. Wang, Y. Xing, R. Lin, X. Wei and W. Wang, *Electrochimica Acta*, 2016, **189**, 245-251

S3.   L. Ma, X.-Y. Pei, D.-C. Mo, S.-S. Lyu and Y.-X. Fu, *Ceramics International*, 2018, **44**, 22664-22670.

S4.   S. M. Abbas, S. T. Hussain, S. Ali, N. Ahmad, N. Ali and S. Abbas, *Journal of Materials Science*, 2013, **48**, 5429-5436.

S5.   Y. Zou, Z. Qi, Z. Ma, W. Jiang, R. Hu and J. Duan, *Journal of Electroanalytical Chemistry*, 2017, **788**, 184-191.

S6.   Q. Xie, L. Lin, Y. Ma, D. Zeng, J. Yang, J. Huang, L. Wang and D.-L. Peng, *Electrochimica Acta*, 2017, **226**, 79-88.

S7.   L. Xiao, E. Li, J. Yi, W. Meng, S. Wang, B. Deng and J. Liu, *Journal of Alloys and Compounds*, 2018, **764**, 545-554.

S8.   S. Li, Y. Xiao, X. Wang and M. Cao, *Physical chemistry chemical physics : PCCP*, 2014, **16**, 25846-25853.

S9.   L. Qie, W. M. Chen, Z. H. Wang, Q. G. Shao, X. Li, L. X. Yuan, X. L. Hu, W. X. Zhang and Y. H. Huang, *Advanced materials*, 2012, **24**, 2047-2050.

S10.   X. H. Huang, X. H. Xia, Y. F. Yuan and F. Zhou, *Electrochimica Acta*, 2011, **56**, 4960-4965.